Mapping subcycle electron motion by modulated high-order harmonic generation

Candong Liu, Zhinan Zeng, Yinghui Zheng, Peng Liu, Ruxin Li, and Zhizhan Xu

Phys. Rev. A **85**, 043420 — Published 24 April 2012

DOI: 10.1103/PhysRevA.85.043420

Mapping sub-cycle electron motion by modulated high-order harmonic generation

Candong Liu, Zhinan Zeng, Yinghui Zheng, Peng Liu, Ruxin Li, and Zhizhan Xu

State Key Laboratory of High Field Laser Physics, Shanghai Institute of Optics and Fine Mechanics, Chinese Academy of Sciences, Shanghai 201800, China

Abstract

We theoretically investigate high-order harmonic generation in argon gas driven by two orthogonally polarized laser pulses of single color, with the consideration of macroscopic propagation effect including fundamental and harmonic field. Both the three-dimensional propagation simulation and a simple analytical model based on singe-atom level demonstrate the harmonic intensity of any harmonic order varies periodically when the delay between two pulses is scanned. This significant intensity modulation provides an experimentally observable contrast, from which the electron excursion time of short quantum path associated with a certain harmonic order can be directly read. The result shows that the attosecond time-resolved electron motion can be mapped onto the macroscopic harmonic intensity modulation

PACS numbers: 42.65.Ky, 32.80.Rm, 42.65.Re

I. INTRODUCTION

Capturing electron dynamics in atoms and molecules is one of the central topics of ultrafast time-resolved measurement [1, 2]. The temporal evolution of the ultrafast process usually calls for isolated attosecond (~100 as) pulses as the probing pulse since the duration is comparable to the Bohr time scale of an electron completing one rotation along Bohr orbit. The electron dynamics in atoms and molecules is often reconstructed by the photoelectron signal induced by this attosecond probing pulse [3, 4].

High-order harmonic generation (HHG) as a nonlinear phenomenon of atoms or molecules subjected to high intensity laser fields has been extensively studied [5]. The underlying dynamics of HHG can be described by the semi-classical three-step model [6]. Not only is HHG used as an approach to generate extreme ultraviolet source for spectroscopic applications, but also itself carries some important information about the electron movement on sub-cycle time scale and spatial structure of ground state [7], as manifested by the third step in the three-step model. Specifically, when the electron recombines with the parent ion core, the fast oscillating dipole as a result of the interference between free electron wave packet and bound state induces the harmonic emission. During this combination process, the electron dynamic information is encoded to characteristics of the emitted photon. It is possible to extract the electron dynamics from the amplitude and phase of emitted harmonic photon by some delicate means, which supplies an alternative tool to implement time-resolved and spatial measurement.

For instance, HHG in aligned molecules has been used for the tomographic imaging of molecular orbit [8]. Two-color and elliptically polarized laser field can not only control and affect the harmonic emission [9-13], but also serve as a temporal gating to identify the harmonic emission time on sub-cycle time scale by measuring harmonic intensity spectrum [14, 15]. Destructive interference during HHG in mixed gases has been experimentally used to identify electron excursion time of short quantum path [16] and observe molecular structure [17]. Since the molecular high harmonic signal is modulated by nuclear vibrational autocorrelation function, HHG can also be used to probe nuclear motion in simple molecules [18-20].

In this paper, we theoretically investigate HHG by using two orthogonally polarized laser pulses of single color, in which one is of high intensity and acts as a driving (pump) pulse, and the other is of low intensity and acts as a modulation (probe) pulse. The probe pulse is weak enough so as to only gently perturb electron trajectory without affecting the ionization induced by the pump pulse. Our main results include: (i) The macroscopic harmonic flux of any harmonic order, which is calculated by non-adiabatic three-dimensional (3D) propagation equation including the evolution of both fundamental and harmonic beams, exhibits a periodic oscillation with scanning the delay between the pump and probe pulse. In the propagation calculation, the focusing geometry and spatial filtering ensure the macroscopic intensity spectrum comes from the contribution of the short quantum path involved in HHG. (ii) A simple analytical model based on saddle-point approximation of single-atom dipole response confirms this kind of oscillation providing an experimentally observable contrast, from which the electron excursion time of short quantum path associated with each harmonic order can be read by a proper inversion algorithm.

II. THEORETICAL MODELS

The high harmonic calculation usually contains two aspects: one is the single-atom response to driving laser field, and the other is the subsequent consideration of macroscopic propagation effect for driving pulse field and the emitted harmonic field. The latter one is especially significant for the reconstruction of experimental results. Solving directly time-dependent Schrödinger equation (TDSE) for the interaction between individual atom and external laser field is the exact way to obtain single-atom response, which is then inserted into Maxwell's wave equation as source term of macroscopic nonlinear polarization. However, it is time-consuming because thousands of TDSEs should be solved when the propagation effect is considered. Instead, the strong-field approximation (SFA) supplies a neat picture to conveniently calculate the single-atom response. The nonlinear dipole moment can be expressed as Lewenstein integral formula (atomic units (a.u.) $e=\hbar=m_e=1$ are used throughout unless otherwise indicated) [21]:

$$\vec{p}(t)=i\int_{-\infty}^{t}dt'[\frac{\pi}{i(t-t')/2}]^{3/2}\vec{E}(t')\bullet\vec{d}(\vec{P_{st}}-\vec{A}(t'))\times e^{-iS_{st}}\vec{d}^{*}(\vec{P_{st}}-\vec{A}(t))a(t)a(t')+c.c\,, \quad (1)$$

where $\vec{E}(t')$ is the electric field, $\vec{A}(t)= -\int_{-\infty}^{t}\vec{E}(t')dt'$ is the vector potential of driving laser field, and the square of $a(t)=\exp(-\int_{0}^{t}w(t')dt'/2)$ refers to the ground-state depletion. We point out the saddle-point approximation momentum is used in this single-atom SFA formula. Here, $w(t')$ is the ionization rate calculated by the ADK model [22, 23]:

$$w(t) = \omega_s \, | c_{n^* l^*} |^2 \, G_{lm} (4\omega_s / \omega_t)^{2n^* - m - 1} \exp(-4\omega_s / 3\omega_t) \, , \qquad (2)$$

where $\omega_s = I_p$, $\omega_t = | E(t) | / \sqrt{2I_p}$, $n^* = Z\sqrt{I_{ph} / I_p}$, $G_{lm} = \dfrac{(2l+1)(l+|m|)!}{2^{|m|} \, |m| ! (l-|m|)!}$, and $| c_{n^* l^*} |^2 = \dfrac{2^{2n^*}}{n^* \Gamma(n^* + l^* + 1) \Gamma(n^* - l^*)}$. Here, I_p is the atomic ionization energy, Z is the net resulting charge of the atom, I_{ph} is the ionization potential of the hydrogen atom, *l* and *m* are angular and magnetic quantum numbers. The effective angular quantum number l^* is $l^* = 0$ for $l << n$, or $l^* = n^* - 1$ otherwise. In Eq. (1), the matrix element for dipole moment transitions from the continuum state to the ground state is given by

$$\vec{d}(\vec{p}) = \frac{i \dfrac{2^{\frac{7}{2}}}{\pi} (2I_p)^{\frac{5}{4}}}{(p^2 + 2I_p)^3} \vec{p} \, , \qquad (3)$$

the stationary momentum is

$$\vec{P_{st}} = \frac{1}{t - t'} \int_{t'}^{t} d\tau \vec{A}(\tau) \, , \qquad (4)$$

and the corresponding stationary quasiclassical action is

$$S_{st} = I_p (t - t') - \frac{1}{2} \vec{P}_{st}^{\,2} (t - t') + \frac{1}{2} \int_{t'}^{t} dt' \vec{A}^2 (t') \, . \qquad (5)$$

Propagation effect is calculated by using a moving coordinate frame and under the slowly-evolving wave approximation, including the evolvement of the fundamental and harmonic beams [24, 25]. The fundamental field propagating in a field-ionizing gas medium is described by

$$\partial_\xi \vec{E}_L = \frac{c}{2}\nabla_\perp^2 \int_{-\infty}^{\tau} dt' \vec{E}_L - \frac{1}{2c}\int_{-\infty}^{\tau} \omega_p^2 \vec{E}_L dt' - \frac{I_p}{2\varepsilon_0 c}\frac{\partial_\tau n_e}{|\vec{E}_L|^2}\vec{E}_L - \frac{\zeta^{(1)}}{c}\partial_\tau n \vec{E}_L, \qquad (6)$$

which contains plasma defocusing effect, self-phase modulation effect and the linear gas dispersion. In Eq. (6), $\omega_p = (n_e/\varepsilon_0)^{1/2}$, n_e, n, c, ε_0 and $\zeta^{(1)}$ refers to the plasma frequency, the density of free electron, the density of neutral atom, the vacuum light speed, the permittivity of free space, and the linear susceptibility of neutral atoms, respectively.

The propagation of harmonic field is described by

$$(\partial_\xi + \alpha_h)\vec{E}_h = \frac{c}{2}\nabla_\perp^2 \int_{-\infty}^{\tau} dt' \vec{E}_h - \frac{1}{2\varepsilon_0 c}\partial_\tau n \vec{p}, \qquad (7)$$

where α_h refers to the absorption of gas target, n is the density of neutral atom, and $\vec{p}$ is the single-atom response calculated by Eq. (1). The two equations can be numerically solved by Crank-Nicholson routine in the frequency domain. The 3D propagation model supplies a robust tool to simulate the real experiment, and can reproduce satisfactorily the experimental results [24-26].

III. RESULTS AND DISCUSSIONS

A. 3D propagation simulation

We consider the typical parameters of a HHG experiment, i.e., a 1-mm-long argon cell at 10 Torr gas pressure is located at the focus of 30-fs Gaussian driving laser pulse with a waist of $25\mu m$, a central wavelength of 800 nm, and a peak intensity of $2\times10^{14} W/cm^2$. Another laser pulse, which is served as a probe pulse, whose polarized direction is perpendicular to the one of driving pulse, has the same duration, waist, and frequency as the driving laser pulse, but a lower peak intensity $2\times10^{12} W/cm^2$. The high harmonics are then generated in these two orthogonal laser fields, which can be easily implemented in the experiment. Multi-optical-cycle driving laser pulse can be directly generated by commercial Ti:sapphire (800nm) laser system, then transmits through a beam splitter to generate the weak probe laser pulse, which can be rotated 90° by a quartz plate.

The delay between the driving pulse and the probe pulse is chosen to an adjustable parameter in our simulation. Both experimental and theoretical studies show that propagation effects can separate long and short electron trajectories in the far-field region [27-32]. In our work, we concentrate on the discussion about the selection of short quantum path. The long quantum path is not filtered in the SFA. The single-atom response calculated by Eq. (1) contains all possible quantum paths. We only make use of propagation effect and spatial filter to automatically select the short quantum path by phase-matching process. This can be confirmed by analyzing the time-frequency behavior of the on-axis harmonics at the exit of the gas cell. The time-frequency analysis approach can be found in Ref. [33]. The calculated time-frequency spectrogram is shown in Fig. 1. One can see that the strong region in the time-frequency spectrogram represents that each harmonic order exhibits a single, approximately linear chirp. This is the case that only one quantum path is dominant in the harmonic spectrum. The contribution from other quantum paths is weak, and therefore can be neglected. Furthermore, the magnitude of the chirp rate, which is described by the slope of the strong region, increases with harmonic order. This is the characteristic of the short quantum path.

Fig. 2(a) shows the macroscopic harmonic intensity spectrum (H25) as a function of the delay from the 3D propagation calculation. The intensity spectrum is obtained by integrating over a narrow region (0~2 mrad) in the far field, which represents that the short quantum path is selected. The far-field harmonics are calculated from the harmonic field at the exit of the gas cell through a Hankel transform [34]. Fig. 2(b) shows each harmonic yield (H21~H31) as a function of the delay. Here, each harmonic yield, which is obtained by integrating over both a spectral window (centered at corresponding central frequency, and a width of 3 eV) and a far-field spatial region (0~2 mrad), is normalized to each corresponding maximum yield. From Fig. 2, one can easily see that the macroscopic harmonic yield varies with a period of half of optical cycle. Another important feature for harmonic yield is that the different harmonic order has the distinct modulation depth, just as shown in Fig. 2(b). We can introduce a macroscopically observable modulation contrast $\beta(\tau_N)$ which corresponds to each harmonic order N and is defined as the ratio between the peak and the valley shown in Fig. 2(b). It is clear that the modulation contrast $\beta(\tau_N)$ increases monotonically with the increase of the harmonic order N. We will show $\beta(\tau_N)$ carries the information on the electron excursion time τ_N of short quantum path associated with harmonic order N in the following text.

B. Analytical investigation

In order to interpret these results shown in Fig. 2, we turn to investigate the underlying dynamics in singe-atom level by further simplifying the integration in

Eq.(1) with saddle-point approximation. To facilitate the description, the driving field and the weak probe field, considered along *x*- and *y*-polarized direction, are expressed as

$$E_x(t) = E_0 \cos(\omega_0 t), \qquad (8a)$$

and

$$E_y(t) = \varepsilon \cos[\omega_0 (t - t_d)], \qquad (8b)$$

where $E_0 = 2\times10^{14} W/cm^2$, $\varepsilon = 2\times10^{12} W/cm^2$, ω_0, and t_d represent the driving field amplitude, the probe field amplitude, the angular frequency, and the delay, respectively. We point out the monochromatic electric field is employed here instead of the multi-optical-cycle Gaussian pulse used in 3D propagation calculation for the convenience of analytical treatment.

For the low intensity of probe pulse ($|\varepsilon|^2 << |E_0|^2$), by substituting both Eq. (8a) and Eq. (8b) into Eq. (1), the atomic dipole moment based on the saddle-point analysis can be described as the sum of the contributions from different electron trajectories [35]:

$$p(t) = \sum_{t_i} \frac{1}{\sqrt{i}} a_{ion}(t_i) a_{pr}(t, t_i) a_{rec}(t) + c.c, \qquad (9)$$

where a_{ion}, a_{pr} and a_{rec} refer to the probability amplitudes of tunneling ionization from ground state, acceleration in the external field and recombination with parent ion core, respectively. It is worth mentioning that the ionization is mainly determined by the driving pulse of high intensity, which indicates the possible electron ionization moment t_i in Eq. (9) is given by the stationary phase equation:

$$A_x(t_i)=\frac{1}{t-t_i}\int_{t_i}^{t}d\tau A_x(\tau)\,.$$

In Eq. (9), the amplitude of tunneling ionization is given by

$$a_{ion}(t_i)=\left(\frac{1}{1+v_{y0}^2(t_i)/2I_p}\right)^{1/2}(2I_p)^{1/2}\exp\left[-\frac{1}{3}\frac{[2I_p+v_{y0}^2(t_i)]^{3/2}}{|E_0|}\right] \qquad (10)$$

Here, the initial lateral velocity is described by

$$v_{y0}(t_i)=-\frac{1}{t_r-t_i}\int_{t_i}^{t_r}d\tau\int_{t_i}^{\tau}E_y(t')dt'\,, \qquad (11)$$

which ensures the electron released at the moment t_i can finally return to the nucleus at the moment t_r in the presence of *y*-direction probe field $E_y(t')$. For $v_{y0}^2(t_i)<<2I_p$ representing the use of sufficiently weak probe field, we can obtain from Eq. (10):

$$|a_{ion}(t_i)|^2\propto\exp\left(-\frac{v_{y0}^2(t_i)}{|E_0|/\sqrt{2I_p}}\right) \qquad (12)$$

With Eq. (8b) and Eq. (11), we have

$$v_{y0}(t_i)\equiv v_{y0}(\tau,\delta)=\frac{\varepsilon}{\omega_0}\left[\frac{\cos[\omega_0(\tau-\delta)]-\cos(\omega_0\delta)}{\omega_0\tau}-\sin(\omega_0\delta)\right]\equiv\varepsilon\theta_{y0}(\tau,\delta)\,, \qquad (13)$$

where $\tau=t_r-t_i$ and $\delta=t_d-t_i$ represent the electron excursion time and delay-relevant variable, respectively.

According to SFA model, when the perpendicularly polarized probe laser $E_y(t)$ joins together in HHG process, the electron emerging in the continuum presents a lateral displacement along *y*-direction. This kind of lateral wave packet diffusion reduces the overlap between the ground state and the free-electron state, consequently leading to the decrease in harmonic intensity. The effect of the weak probe field on high harmonic generation can be viewed as a perturbation process.

Since the electron ionization event takes place in every half-optical-cycle of the driving pulse, in Eq. (9) the two adjacent ionization moments t_i associated with harmonic order N has an interval of π / ω_0. Note that we only consider short quantum path here. By combining Eq. (9), Eq. (12) and Eq. (13), we can obtain the perturbed Nth harmonic intensity: (Note that $v_{y0}^2(\tau_N, \delta) = v_{y0}^2(\tau_N, \delta \pm \pi / \omega_0)$)

$$I(\tau_N, \delta) = I_{N,\varepsilon=0} \exp(-v_{y0}^2 / v_0^2), \qquad (14)$$

where τ_N, $I_{N,\varepsilon=0}$, and $v_0 = \sqrt{|E_0| / \sqrt{2I_p}}$ represent the electron excursion time corresponding to harmonic order N, the unperturbed Nth harmonic intensity without the probe laser field, and the lateral velocity bandwidth, respectively.

From Eq. (14), for a given harmonic order N, one can easily see the harmonic intensity satisfying $I(\tau_N, \delta) = I(\tau_N, \delta \pm \pi / \omega_0)$ varies periodically from the maximum (peak) to the minimum (valley) with scanning the delay, which provides a good explanation to the results in Fig. 2. The maximum and minimum harmonic intensity can be obtained by the saddle-point equation:

$$\partial_\delta I(\tau_N, \delta) = 0, \qquad (15)$$

which gives two separate equations:

$$\frac{\sin[\omega_0(\tau_N - \delta_{\min})] + \sin(\omega_0 \delta_{\min})}{\omega_0 \tau_N} = \cos(\omega_0 \delta_{\min}) \qquad (16)$$

and

$$\frac{\cos[\omega_0(\tau_N - \delta_{\max})] - \cos(\omega_0 \delta_{\max})}{\omega_0 \tau_N} = \sin(\omega_0 \delta_{\max}). \qquad (17)$$

The relationship between τ_N and δ described by Eq. (16) and Eq. (17) gives those delays which generate the minimum harmonic intensity $I_{\min}$=$I(\tau_N, \delta_{\min})$ and the maximum harmonic intensity $I_{\max} = I(\tau_N, \delta_{\max})$, respectively. Therefore, the contrast of the Nth harmonic intensity modulation is given by:

$$\beta(\tau_N) = \frac{I_{\max}}{I_{\min}} = \frac{I(\tau_N, \delta_{\max})}{I(\tau_N, \delta_{\min})}. \tag{18}$$

By numerically solving both Eq. (16) and Eq. (17), and substituting the solution into Eq. (18), we can obtain the contrast $\beta(\tau_N)$, just as shown in Fig. 3(a). Fig. 3(b) shows harmonic photon energy as a function of the corresponding electron excursion time τ, which is calculated by quantum theory [21]. We can see from Fig. 3(a) and Fig. 3(b), the different harmonics have the different contrast when the delay between driving pulse and probe pulse is scanned. In particular, for the short quantum path discussed in our work, the contrast increases with the increase of the harmonic order. Therefore, our analytical model gives the result consistent with Fig. 2(b).

Additionally, we point out the weak probe field can not significantly affect the action. In our work, the polarized direction of the weak probe field is perpendicular to the one of the strong driving field. Therefore, the exact action can be expressed as $S{=}S_1{+}\sigma$, where S_1 is the approximated action only including the contribution of the strong driving field, and σ is the additional phase induced by the weak probe field. Using the saddle-point analysis method, we can calculate the electron excursion time associated with different harmonics under two cases: (i) using the exact action S, and (ii) using the approximated action S_1. For S and S_1, the corresponding excursion time of short quantum path is denoted as $T(q)$ and $T_1(q)$, respectively. The relative change rate of the excursion time associated with harmonic order q can therefore be defined by $\frac{T(q)-T_1(q)}{T_1(q)}$, which is shown by Fig. 4. It is found that the relative change rate is less than 1% for the harmonic order H21~H31. Thus, it is reasonable for the use of the approximated action S_1 to describe the phase of the acceleration. We also estimate the harmonic intensity in the y-direction is two orders of magnitude lower than the one in the x-direction, which represents the harmonics emitted in the perpendicular direction is not important.

C. Retrieval of the electron excursion time

We can see from Eq. (14), the electron excursion time associated with a certain harmonic order N is encoded to the corresponding harmonic intensity modulation. Thus, it supplies an opportunity to retrieve the electron excursion time by a proper inversion formula. We start from Eq. (18) and describe how to read the electron excursion time, as follows:

For a given harmonic order N, according to Eq. (13), Eq. (14) and Eq. (17), the maximum harmonic intensity $I(\tau_N, \delta_{\max})$ satisfies:

$$I(\tau_N, \delta_{\max}) = I_{N,\varepsilon=0} \tag{19}$$

With Eq. (13), Eq. (14), Eq. (18), and Eq. (19), we have

$$\frac{v_0}{\varepsilon}\sqrt{\ln \beta(\tau_N)} = \theta_{y0}(\tau_N, \delta_{\min}), \tag{20}$$

where τ_N and $\delta_{\min}$ is coupled by Eq. (16). In order to eliminate the dependence on v_0 / ε in Eq. (20), $\theta_{y0}(\tau_N, \delta_{\min})$ is normalized to $\theta_{y0}(\tau_{N_0}, \delta_{\min})$ corresponding to a certain harmonic order N_0. In this way, we have

$$\sqrt{\ln\beta(\tau_N)/\ln\beta(\tau_{N_0})} = \theta_{y0}(\tau_N,\delta_{\min})/\theta_{y0}(\tau_{N_0},\delta_{\min}) \tag{21}$$

The response of $\theta_{y0}(\tau,\delta_{\min})/\theta_{y0}(\tau_{N_0},\delta_{\min}) \equiv \theta(\tau;\tau_{N_0})$ calculated from both Eq. (13) and Eq. (16) is shown in Fig. 5(b), where we set $N_0 = 25$. It is worth mentioning here that the function $\theta(\tau;\tau_{N_0})$ represents the intrinsic dynamics of electron wave packet lateral diffusion, which is independent of the probe laser intensity and the atomic ionization energy.

By using the macroscopic modulation contrast $\beta(\tau_N)$ directly obtained from Fig. 2(b), we can calculate $\theta(\tau_{\mathrm{N}};\tau_{25}) = \sqrt{\ln\beta(\tau_N)/\ln\beta(\tau_{25})}$, which represents an observable variable in the experiment. The calculated result is shown in Fig. 5(a), while Fig. 5(b) presents the generally intrinsic response $\theta(\tau_{\mathrm{N}};\tau_{25})$ calculated by the analytical model. By comparing Fig. 5(a) and Fig. 5(b), we can retrieve the electron excursion time associated with each harmonic order. The reconstructed excursion time is represented by circles in Fig. 5(c), in which solid line presents the calculated excursion time by quantum theory [21].

Fig. 5(c) shows the electron excursion time is obtained by two different ways. One (circles) is obtained by the inversion algorithm making use of macroscopically observable harmonic intensity modulation. The other (solid line) is obtained by direct quantum theory of single-atom model. One can find that both results are coincident, which demonstrates that the sub-cycle electron motion can be read from the modulation of macroscopic harmonic spectrum.

The focal volume of the two laser fields for the retrieval is important. The perturbed harmonic intensity is sensitive to the weak field intensity through the exponential relationship just as shown by Eq. (14). Moreover, the spatial filter is used in our work to only select the harmonics near the axis. Therefore, in order to make the retrieval algorithm useful, the non-uniformity of laser intensity along the on-axis direction should be reduced by making the Rayleigh length of the driving and the probe laser pulse longer than the gas target length.

Finally, the effect of the propagation calculation on the retrieval algorithm is worth mentioning. In our work, we mainly discuss the retrieve of electron excursion time associated with short quantum path. The harmonic spectrum from single-atom calculation includes the total contribution from the short and the long quantum path. Although we can only pick out the short quantum path by the mathematical treatment for SFA formula, however this is not a real physical case. On the contrary, the propagation of harmonics provides a real process to select the short quantum path, which is automatically achieved by phase-matching effect. As a result, the harmonic field from the short quantum path is dominant on the axis at the exit of the gas cell even if the singe-atom calculation includes the contribution of all possible quantum paths. This kind of selection is the same as the real experiment. Propagation calculation used here can be viewed as a simulation for HHG experiment. Therefore, the feasibility of our scheme is demonstrated due to the fact that the harmonic signal used for the retrieve of electron excursion time is not from the single-atom calculation but from the macroscopic propagation process.

IV. CONCLUSION

The two orthogonally polarized laser fields constructed by a high-intensity driving pulse and a low-intensity probe field with the same central frequency are proposed to map the sub-cycle electron dynamics during HHG process. The effect of the probe pulse is reflected in the generation of modulated harmonic intensity. Taking into account both the non-adiabatic 3D propagation calculation and the single-atom analytical model, we demonstrate the intensity spectrum of any harmonic order exhibits a periodic oscillation from the maximum to the minimum with scanning the delay between the driving pulse and the probe pulse. Our propagation calculations can be viewed as a simulation experiment, which supplies a macroscopically observable modulation contrast. By using the macroscopic contrast and the intrinsic response of electron wave packet lateral diffusion, we successfully retrieve the electron excursion time of short quantum path associated with the harmonic order H21~H31. The result shows the sub-cycle electron motion is mapped onto the modulation of macroscopic harmonic intensity, and therefore can be directly read by a proper inversion algorithm.

Acknowledgements

We acknowledge the support from National Natural Science Foundation of China (Grant Nos. 10734080, 60578049, 10523003), National Basic Research Program of China (Grant No. 2006CB806000), Chinese Academy of Sciences, State Key Laboratory Program of Chinese Ministry of Science and Technology.

Corresponding authors: ruxinli@mail.shcnc.ac.cn, zzxu@mail.shcnc.ac.cn.

References:

[1] P. Agostini and L. F. DiMauro, Rep. Prog. Phys. **67**, 813 (2004).

[2] G. A. Reider, J. Phys. D: Appl. Phys. **37**, R37 (2004).

[3] T. Morishita, S. Watanabe, and C. D. Lin, Phys. Rev. Lett. **98**, 083003 (2007).

[4] E. Goulielmakis, Z. Loh, A. Wirth, R. Santra, N. Rohringer, V. S. Yakovlev, S. Zherebtsov, T. Pfeifer, A. M. Azzeer, M. F. Kling, S. R. Leone and F. Krausz, Nature (London) **466**, 739 (2010).

[5] F. Krausz and M. Ivanov, Rev. Mod. Phys. **81**, 163 (2009).

[6] P. B. Corkum, Phys. Rev. Lett. **71**, 1994 (1993).

[7] P. B. Corkum, and F. Krausz, Nature physics **3**, 381 (2007).

[8] J. Itatani, J. Levesque, D. Zeidler, H. Niikura, H. Pépin, J. C. Kieffer, P. B. Corkum, and D. M. Villeneuve, Nature (London) **432**, 867 (2004).

[9] D. B. Milošević and W. Becker Phys. Rev. A **62**, 011403 (2000).

[10] M. Kitzler, X. Xie, S. Roither, A. Scrinzi, and A. Baltuska, New J. Phys. **10**, 025029 (2008).

[11] C. Ruiz, D. J. Hoffmann, R. Torres, L. E. Chipperfield, and J. P. Marangos, New J. Phys. **11**, 113045 (2009).

[12] F. A. Weihe, S. K. Dutta, G. Korn, D. Du, P. H. Bucksbaum, and P. L. Shkolnikov, Phys. Rev. A **51**, R3433 (1995).

[13] K. S. Budil, P. Salières, M. D. Perry, and A. L'Huillier, Phys. Rev. A **48**, R3437 (1993).

[14] N. Dudovich, O. Smirnova, J. Levesque, Y. Mairesse, M. Yu. Ivanov, D. M.

Villeneuve and P. B. Corkum, Nature Physics **2**, 781 (2006).

[15] N. Dudovich, J. Levesque, O. Smirnova, D. Zeidler, D. Comtois, M. Yu. Ivanov, D. M. Villeneuve, and P. B. Corkum, Phys. Rev. Lett. **97**, 253903 (2006).

[16] T. Kanai, E. J. Takahashi, Y. Nabekawa, and K. Midorikawa., Phys. Rev. Lett. **98**, 153904 (2007).

[17] T. Kanai, E. J. Takahashi, Y. Nabekawa, and K. Midorikawa, Phys. Rev. A **77**, 041402(R) (2008).

[18] M. Lein, Phys. Rev. Lett, **94**, 053004 (2005).

[19] S. Baker, J. S. Robinson, C. A. Haworth, H. Teng, R. A. Smith, C. C. Chirilă, M. Lein, J. W. G. Tisch, and J. P. Marangos, Science **312**, 424 (2006).

[20] C. Liu, Z. Zeng, P. Wei, P. Liu, R. Li, and Z. Xu, Phys. Rev. A. **81**, 033426 (2010).

[21] M. Lewenstein, Ph. Balcou, M. Yu. Ivanov, A. L'Huillier, and P. B. Corkum, Phys. Rev. A **49**, 2117 (1994).

[22] M. V. Ammosov et al., Zh. Eksp. Tero. Fiz. **91**, 2008 (1986) [Sov. Phys. JETP **64**, 1191 (1986)].

[23] M. Protopapas, C. H. Keitel and P. L. Knight, Rep. Prog. Phys. **60**, 389 (1997).

[24] E. Priori, G. Cerullo, M. Nisoli, S. Stagira, and S. De Silvestri, Phys. Rev. A **61**, 063801 (2000).

[25] N. Milosevic, A. Scrinzi, and T. Brabec, Phys. Rev. Lett. **88**, 093905 (2002).

[26] F. Ferrari, F. Calegari, M. Lucchini, C. Vozzi, S. Stagira, G. Sansone and M. Nisoli, Nature Photonics **4**, 875 (2010).

[27] M. Lewenstein, P. Salières, and A. L'Huillier, Phys. Rev. A **52**, 4747 (1995).

[28] P. Antoine, A. L'Huillier, and M. Lewenstein, Phys. Rev. Lett. **77**, 1234 (1996).

[29] C. Liu, Y. Zheng, Z. Zeng, R. Li, and Z. Xu, Phys. Rev. A **79**, 043826 (2009).

[30] C. Liu, Y. Zheng, Z. Zeng, P. Liu, R. Li, and Z. Xu, Opt. Express **17**, 10319 (2009).

[31] C. Liu, R. Li, Z. Zeng, Y. Zheng, P. Liu, and Z. Xu, Opt. Lett. **35**, 2618 (2010).

[32] H. Merdji, M. Kovačev, W. Boutu, P. Salières, F. Vernay, and B. Carré, Phys. Rev. A **74**, 043804 (2006).

[33] Mette B. Gaarde, Opt. Express **8**, 529 (2001)

[34] V. Tosa, K. T. Kim, and C. H. Nam, Phys. Rev. A **79**, 043828 (2009).

[35] M. Yu. Ivanov, T. Brabec, and N. Burnett, Phys. Rev. A **54**, 742 (1996).

Figure Captions:

FIG. 1. (Color online) Time-frequency behavior of the on-axis harmonics at the exit of the gas cell.

FIG. 2. (Color online) (a) Macroscopic 25th harmonic spectrum as a function of the delay. The intensity spectrum is obtained by integrating over a narrow spatial region (0~2 mrad) in the far field. (b) Macroscopic 21st~31st harmonic yield as a function of the delay. The harmonic yield, calculated by integrating over both a spectral window (centered at corresponding central frequency, and a width of 3 eV) and a far-field spatial region (0~2 mrad), is normalized to each corresponding maximum yield.

FIG. 3. (Color online) (a) The contrast $\beta(\tau)$ as a function of electron excursion time τ. It is obtained from Eq. (18). (b) Harmonic energy as a function of the corresponding electron excursion time τ. Short quantum path corresponds to $\tau < 4.08$, and long quantum path corresponds to $\tau > 4.08$.

FIG. 4. (Color online) The relative change rate of the electron excursion time obtained from the exact action S and the approximated action S_1 as a function of harmonic order.

FIG. 5. (Color online) Reconstruction of the electron excursion time associated with H21~H31. (a) Macroscopic response of $\theta(\tau_{\mathrm{N}};\tau_{25}) = \sqrt{\ln\beta(\tau_N)/\ln\beta(\tau_{25})}$ as a function of harmonic order. $\beta(\tau_N)$ is directly read from Fig. 2(b). (b) Generally intrinsic response of $\theta(\tau_{\mathrm{N}};\tau_{25})$ as a function of electron excursion time. It is calculated with the analytical model and independent of probe laser

intensity and atomic potential. (c) Reconstructed excursion time (colorized circles) together with theoretical curve (solid line) calculated by quantum theory.

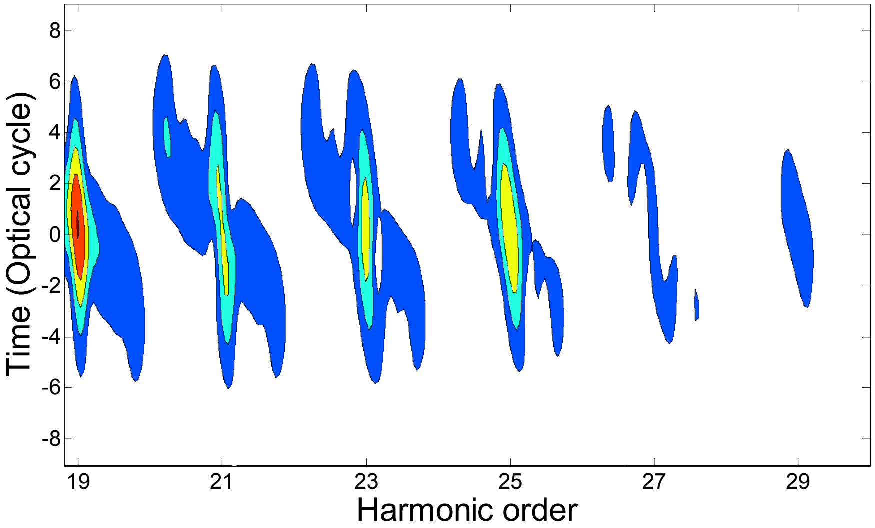

FIG. 1. (Color online) Time-frequency behavior of the on-axis harmonics at the exit of the gas cell.

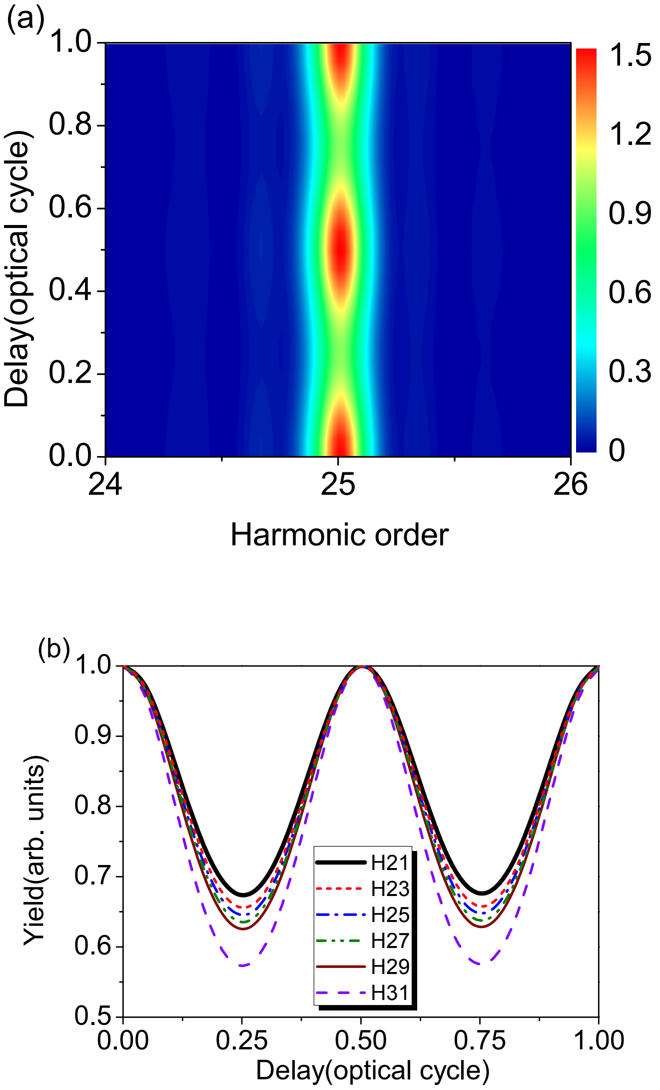

FIG. 2. (Color online) (a) Macroscopic 25th harmonic spectrum as a function of the delay. The intensity spectrum is obtained by integrating over a narrow spatial region (0~2 mrad) in the far field. (b) Macroscopic 21st~31st harmonic yield as a function of the delay. The harmonic yield, calculated by integrating over both a spectral window (centered at corresponding central frequency, and a width of 3 eV) and a far-field spatial region (0~2 mrad), is normalized to each corresponding maximum yield.

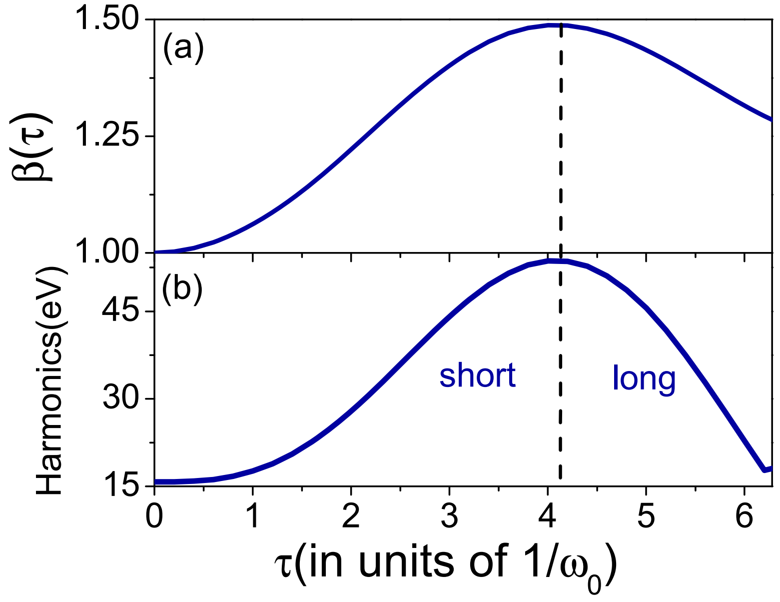

FIG. 3. (Color online) (a) The contrast $\beta(\tau)$ as a function of electron excursion time τ. It is obtained from Eq. (18). (b) Harmonic energy as a function of the corresponding electron excursion time τ. Short quantum path corresponds to $\tau < 4.08$, and long quantum path corresponds to $\tau > 4.08$.

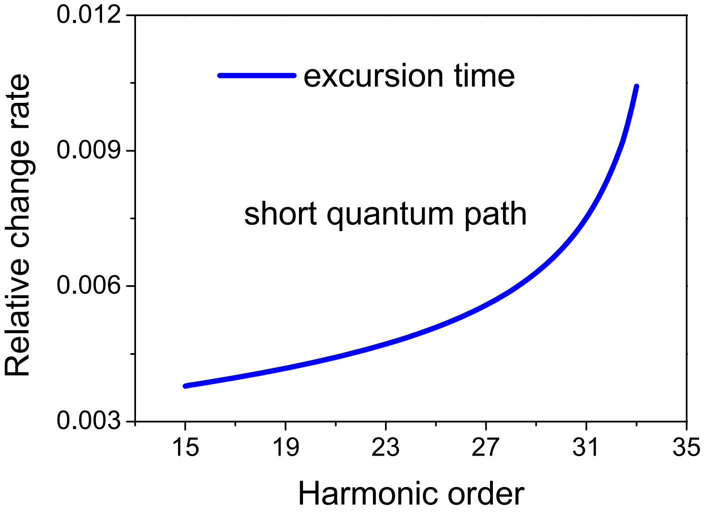

FIG. 4. (Color online) The relative change rate of the electron excursion time obtained from the exact action S and the approximated action S_1 as a function of harmonic order.

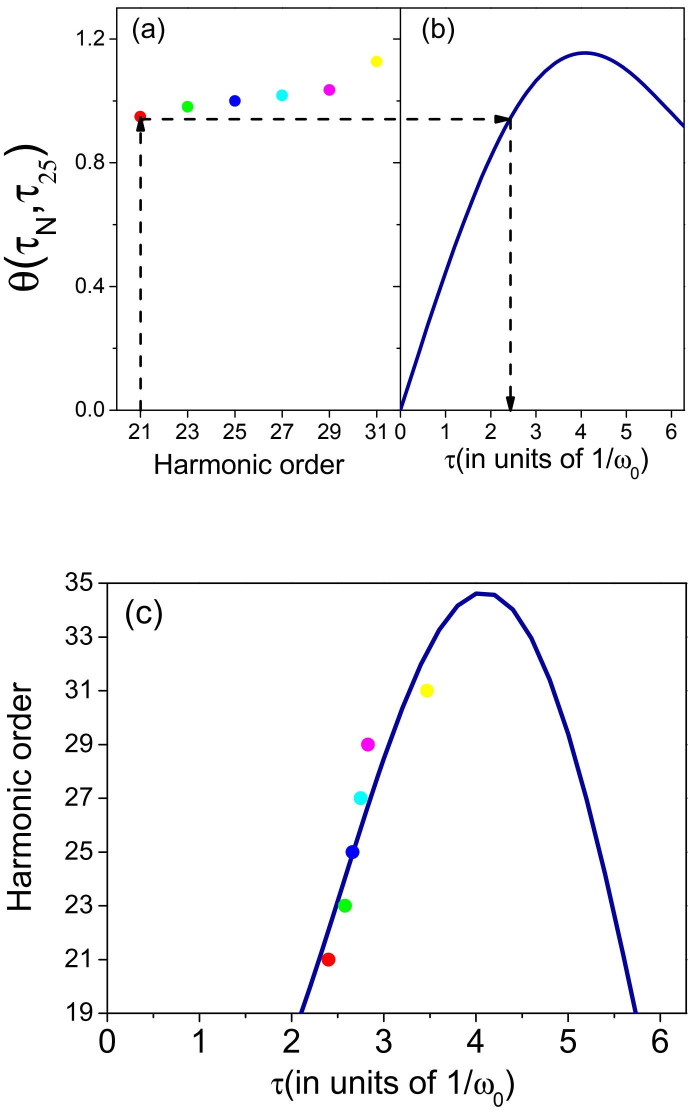

FIG. 5. (Color online) Reconstruction of the electron excursion time associated with H21~H31. (a) Macroscopic response of $\theta(\tau_{\mathrm{N}};\tau_{25})=\sqrt{\ln\beta(\tau_N)/\ln\beta(\tau_{25})}$ as a function of harmonic order. $\beta(\tau_N)$ is directly read from Fig. 2(b). (b) Generally intrinsic response of $\theta(\tau_{\mathrm{N}};\tau_{25})$ as a function of electron excursion time. It is calculated with the analytical model and independent of probe laser intensity and atomic potential. (c) Reconstructed excursion time (colorized circles) together with theoretical curve (solid line) calculated by quantum theory.